ELECTROCHEMISTRY

Fundamental mechanistic insights into the catalytic reactions of Li—S redox by Co single-atom electrocatalysts via operando methods

Weixuan Xu[1]†, Shuangyan Lang[1]*†, Kaiyang Wang[2], Rui Zeng[1], Huiqi Li[1], Xinran Feng[1], Mihail R. Krumov[1], Seong-Min Bak[3], Christopher J. Pollock[4], Jingjie Yeo[5], Yonghua Du[6], Héctor D. Abruña[1]*

Lithium-sulfur batteries represent an attractive option for energy storage applications. A deeper understanding of the multistep lithium-sulfur reactions and the electrocatalytic mechanisms are required to develop advanced, high-performance batteries. We have systematically investigated the lithium-sulfur redox processes catalyzed by a cobalt single-atom electrocatalyst (Co-SAs/NC) via operando confocal Raman microscopy and x-ray absorption spectroscopy (XAS). The real-time observations, based on potentiostatic measurements, indicate that Co-SAs/NC efficiently accelerates the lithium-sulfur reduction/oxidation reactions, which display zero-order kinetics. Under galvanostatic discharge conditions, the typical stepwise mechanism of long-chain and intermediate-chain polysulfides is transformed to a concurrent pathway under electrocatalysis. In addition, operando cobalt K-edge XAS studies elucidate the potential-dependent evolution of cobalt's oxidation state and the formation of cobalt-sulfur bonds. Our work provides fundamental insights into the mechanisms of catalyzed lithium-sulfur reactions via operando methods, enabling a deeper understanding of electrocatalysis and interfacial dynamics in electrical energy storage systems.

INTRODUCTION

Lithium-sulfur (Li—S) batteries are widely considered as one of the most promising electrical energy storage systems because of their high theoretical energy density (2600 Wh kg^{-1}), their low cost, and the environmental friendliness of S (*1*–*4*). However, the commercial viability is still hindered by several challenges. The insulating nature of S and discharged products (Li_2S/Li_2S_2) precludes the electrochemical accessibility and full utilization of the active material, especially at high C-rates. In addition, the large volumetric change of the S electrode during charge/discharge processes can compromise the integrity of the electrode and degrade cell performance. More critically, the "polysulfide shuttle effect" caused by soluble intermediate lithium polysulfides (LiPSs) can lead to the loss of active material from the S electrode and poor Coulombic efficiency, as well as the corrosion of the Li metal anode, resulting in passivation of the electrode and rapid capacity fade (*5*–*7*). Considerable efforts have been devoted to mitigating the polysulfide shuttle, typically by physical confinement using porous carbonaceous materials [e.g., mesoporous carbon (*8*) and metal-organic framework (MOF)–derived carbon (*9*, *10*)] and via chemical binding with polar materials [e.g., metal oxides (*11*, *12*), metal sulfides (*13*, *14*), and heteroatom dopants in carbon matrices (*15*)]. In addition, electrolyte additives (e.g., $LiNO_3$) are able to suppress the shuttle effect by forming a uniform passivation film, called a solid electrolyte interface, on the surface of the Li anode (*16*, *17*).

While substantial progress has been made, the challenges associated with the S electrode still persist because of the intrinsic sluggish kinetics of the solid-liquid-solid (S-LiPSs-Li_2S) phase transformations during Li—S redox processes (*18*). Electrocatalysis is a promising strategy to accelerate the multistep reactions in Li—S batteries, mitigate the accumulation of soluble LiPSs in the electrolyte, and thus improve cycle life. Metal nanoparticles (*19*, *20*), transition metal compounds [e.g., oxides (*21*, *22*), sulfides (*14*, *23*), and nitrides (*24*, *25*)], and heteroatoms doped into carbon materials (*26*–*28*) have been used as electrocatalysts to accelerate the reaction kinetics of Li—S batteries. Single-atom catalysts (SACs), with well-dispersed metal atoms on designed substrates, represent one of the most promising electrocatalysts because of the theoretical 100% atom utilization efficiency and combined advantages of homogeneous and heterogeneous catalysts (*29*, *30*). SACs with TM—N—C (TM = Co, Fe, V, and Ni) formation exhibit high polarity for LiPS adsorption and great potential for enhancing the reaction kinetics (*31*–*33*). However, mechanistic studies of electrocatalysis in Li—S batteries have not mirrored the recent advances in developing high-performance catalysts with optimized structures. The limited efforts at unveiling electrocatalytic mechanisms are linked to the difficulties of dynamically tracking the multistep Li—S redox reactions, definitively identifying active-site structures and accounting for active-site heterogeneity. The real-time monitoring of active sites is particularly challenging, even for relatively simple systems of SACs with well-defined architectures, because of the ultralow concentration of single-atom sites. Advanced techniques with high sensitivity and sufficient time resolution are critical for gaining a comprehensive understanding of Li—S redox processes and electrocatalytic mechanisms in operating cells.

[1]Department of Chemistry and Chemical Biology, Cornell University, Ithaca, NY 14853, USA. [2]Department of Materials Science and Engineering, Cornell University, Ithaca, NY 14853, USA. [3]Department of Materials Science and Engineering, Yonsei University, Seoul 03722, Republic of Korea. [4]Cornell High Energy Synchrotron Source, Wilson Laboratory, Cornell University, Ithaca, NY, 14853, USA. [5]Sibley School of Mechanical and Aerospace Engineering, Cornell University, Ithaca, NY 14853, USA. [6]National Synchrotron Light Source II, Brookhaven National Laboratory, Upton, NY 11973, USA.
*Corresponding author. Email: sl3336@cornell.edu (S.L.); hda1@cornell.edu (H.D.A.)
†These authors contributed equally to this work.

Over the past few decades, intense efforts have been pursued to develop in situ/operando characterization techniques with the aim of providing spatiotemporally resolved insights into Li—S batteries (*34*, *35*). Confocal Raman microscopy enables the simultaneous detection of S and polysulfides with different chain lengths, as well as obtaining high-resolution images to directly visualize S speciation (*36*). Our group previously used operando confocal Raman microscopy to investigate and quantify Li—S redox processes, revealing the first-order kinetics of S reduction and polysulfide redox processes, as well as the stepwise discharge and parallel recharge mechanism of polysulfides (*37*). Synchrotron-based methods, including x-ray absorption spectroscopy (XAS) (*38*–*41*), x-ray diffraction (XRD) (*42*, *43*), and x-ray microscopy (*44*, *45*), represent additional powerful techniques to distinguish different S species and unveil their transformation pathways in discharge-recharge processes. In earlier work, Cuisinier *et al*. (*38*) monitored S speciation and revealed the mechanisms of S redox chemistry on cycling via operando XAS of the S K-edge. In addition, atomic force microscopy (*46*, *47*), nuclear magnetic resonance (*48*, *49*), electron microscopy (*50*, *51*), and ultraviolet-visible (UV-vis) spectroscopy (*52*, *53*) have provided additional invaluable dynamic information on Li—S cells. Despite numerous reports on in situ/operando methods for Li—S batteries, there is limited understanding of electrocatalyzed Li—S redox reactions, especially by SACs. Thus, their catalytic pathways and mechanisms remain elusive.

Here, a MOF-derived material with atomically dispersed cobalt (Co) atoms on a nitrogen (N)–doped carbon support (denoted as Co-SAs/NC) was used as a cathode electrocatalyst in Li—S batteries. Combined with operando confocal Raman microscopy and operando XAS of the S K-edge, we have systematically investigated the reaction kinetics and mechanisms of Co-SAs/NC–catalyzed Li—S redox reactions under potentiostatic conditions as well as galvanostatic discharge-recharge processes. By direct visualization and quantitative analysis of the potential-dependent reactants and intermediates, we demonstrate the zero-order kinetics of S reduction and polysulfide oxidation processes in the presence of Co-SAs/NC, which is markedly different from the first-order kinetics in the noncatalyzed case. During galvanostatic discharge-recharge processes, Raman images of the surface region and deep into the electrolyte were obtained, fully displaying the S speciation in both *XY* and *XZ* planes. The concurrent evolution trends of long-chain (S_x^{2-}, x = 6 to 8) and intermediate-chain (S_x^{2-}, x = 3 to 5) polysulfides illustrate the accelerated kinetics of the multistep polysulfide transitions catalyzed by Co-SAs/NC, which are further confirmed by evidence from operando XAS of S K-edge. In addition, operando XAS measurements of the Co K-edge were performed to capture dynamic changes of electronic structure and local environment of the Co atoms in the Co-SAs/NC catalysts, revealing the nature of the active site and tracking its changes during Li—S redox. Our work focuses on the real-time monitoring of the dynamic evolution of the reactants (S species) and catalysts (Co-SAs/NC) via operando methods and provides an integrative understanding of the facilitated kinetics and electrocatalytic mechanisms of Li—S redox reactions with single-atom electrocatalysts. They establish a systematic and methodological framework to decipher reaction mechanisms and could inform and enable detailed exploration of complex pathways in other state-of-the-art sustainable electrical energy storage systems.

RESULTS AND DISCUSSION

Structural and electrochemical characterization of Co-SAs/NC

The Co single atoms supported on an N-doped carbon, denoted as Co-SAs/NC, were prepared from MOF-$Zn_{20}Co$ precursors by heat treatment under forming gas (H_2 + N_2) flow (see Materials and Methods for details). As control groups, Co nanoparticles supported on N-doped carbon (Co-NPs/NC) and N-doped carbon (NC) were prepared from MOF-Zn_xCo_y as well by adjusting the Zn/Co ratio (x/y). As shown in figs. S1 to S3, the crystalline structures, morphologies, and electronic states of synthesized Co-SAs/NC materials were identified by XRD, aberration-corrected high-angle annular dark-field scanning transmission electron microscopy (HAADF-STEM) along with electron energy loss spectroscopy (EELS) elemental mapping, and x-ray photoelectron spectroscopy (XPS), respectively. The characterization results revealed the atomic dispersion of Co atoms on the MOF-derived carbon substrates and suggested a Co—N_x local configuration in Co-SAs/NC.

Cyclic voltammetry (CV) was carried out to assess the catalytic activity of Co-SAs/NC in Li—S batteries. The catalytic effect of Co-SAs/NC, on the electrochemical conversion of LiPSs, was evaluated via symmetric cells in an electrolyte of 0.5 M Li_2S_6 in the solvent mixture of 1,3-dioxolane (DOL)/1,2-dimethoxyethane (DME) (1:1, v/v) (fig. S4). Compared to Co-NPs/NC and NC, Co-SAs/NC showed smaller voltage hysteresis between the anodic and cathodic peaks, implying its superior catalytic effect on the conversion of LiPSs. In Li—S cells with an S@catalyst cathode and Li anode, Co-SAs/NC exhibited enhanced reaction kinetics for Li—S redox processes and delivered a higher discharge capacity, compared to the Co-NPs/NC and NC catalysts, as shown in figs. S5 and S6. To unveil the reaction mechanisms of Co-SAs/NC–catalyzed Li—S redox processes, operando confocal Raman microscopy and XAS were carried out.

Kinetics of potentiostatic reduction/oxidation reactions catalyzed by Co-SAs/NC

In a typical electrolyte of 1.0 M lithium bis(trifluoromethanesulfonyl)imide (LiTFSI) in DOL/DME (1:1, v/v), the reduction of S involves the ring opening of S_8 and subsequent chain shortening processes of polysulfides (L_2S_x): long chain (x = 6 to 8) → intermediate chain (x = 3 to 5) → short chain (x = 1 to 2) (*54*, *55*). Figure 1 shows the operando confocal Raman microscopy study of the potentiostatic reduction of S clusters under the catalytic effects of Co-SAs/NC. A chronoamperometric measurement was conducted at an applied potential of 2.25 V (versus Li/Li^+), representing an overpotential (η) of ~120 mV compared with the open-circuit voltage (E_{relax} = 2.37 V) of the first plateau in the galvanostatic intermittent titration technique profile (fig. S7). Figure 1A presents the current as a function of time (*i*-*t* curve). Raman spectra are presented in Fig. 1B. The characteristic Raman peaks at 152, 219, and 473 cm^{-1} are ascribed to elemental S (S_8) (*56*). During the reduction process, these peaks decreased followed by the emergence of two peaks at 398 and 450 cm^{-1}, which were assigned to long-chain polysulfides (Li_2S_x, x = 6 to 8) and intermediate-chain polysulfides (Li_2S_x, x = 3 to 5), respectively (*55*, *57*), indicating the evolution from elemental S to polysulfides.

The optical images and Raman mappings collected during the S potentiostatic reduction process are presented in fig. S8 and Fig. 1C,

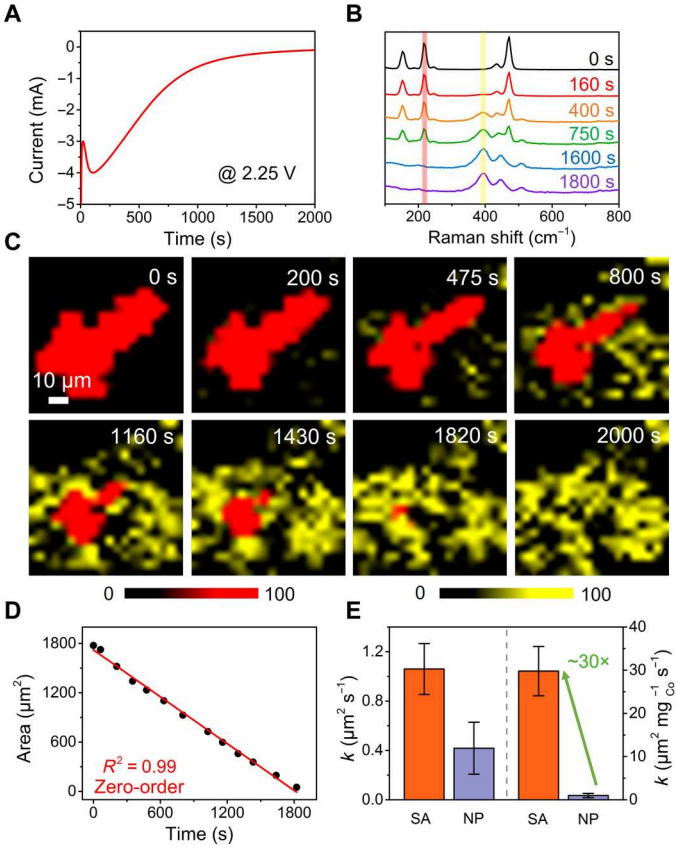

Fig. 1. Operando confocal Raman study of the potentiostatic reduction of S catalyzed by Co-SAs/NC. (**A**) Chronoamperometric current-time (*i-t*) transient of S reduction at 2.25 V (versus Li/Li$^+$) with Co-SAs/NC catalysts. Operando Raman (**B**) spectra and (**C**) mapping images of the S electrode during reduction catalyzed by Co-SAs/NC. The red and yellow colors in (C) represent S and long-chain polysulfides, respectively, where the color contrasts remained consistent for quantification. (**D**) Plot of the area changes of S clusters with time. (**E**) Values of *k* and normalized *k* into the mass of Co derived from S reduction processes catalyzed by Co-SAs/NC and Co-NPs/NC, respectively.

respectively. The Raman video of the reduction process is included in the Supplementary Materials (movie S1). The Raman mappings were captured in an 80 μm by 80 μm region and constructed from the bands at 219 cm^{-1} (red, S) and 398 cm^{-1} (yellow, long-chain polysulfides) in the Raman spectra (Fig. 1B), respectively. The S cluster dissolved from the edges to the center and fully disappeared at 2000 s, while the polysulfides became evident gradually after 200 s and were dominant in the mapping at 2000 s. In an effort to explore the kinetics of the potentiostatic reduction of S, the corresponding area changes of the S cluster in the Raman mappings were plotted as a function of time (Fig. 1D), where the active surface area of S was represented by the projected area from the Raman mapping. The reaction rate of S reduction can be expressed by the following equation

$$-\frac{dA}{dt} = kA^n \quad (1)$$

where A represents the active surface area of S calculated from Raman mapping, which we assume as a proxy for the concentration; t is the reaction time; k represents the rate constant for the reduction of S; and n is the reaction order with respect to S. In the presence of Co-SAs/NC, the plot of the area of S (A) versus time (t) exhibited a linear relationship with an R^2 of 0.99, where the reaction rate was constant and did not vary with the decrease in S. Thus, the reduction of S catalyzed by Co-SAs/NC represents a zero-order kinetics (n = 0) process. Such behavior has been widely studied in enzyme-catalyzed reactions (*58*, *59*). The corresponding reaction rate expression can be written as

$$-\frac{dA}{dt} = k_{\mathrm{Co-SA}} \quad (2)$$

where $k_{\mathrm{Co\text{-}SA}}$ represents the rate constant for the S reduction reaction catalyzed by Co-SAs/NC. In addition, as shown in fig. S9, different order kinetics were tried to fit the data. The fittings for the first-, second-, and third-order kinetics were poor with R^2 values of 0.83, 0.37, and 0.21, respectively. These are clearly much poorer fits when compared to the zero-order kinetic analysis. The previous work has showed that, without any catalysts, the potentiostatic reduction of S is a first-order reaction process, in which the reaction rate decreases with the decreasing active area of S (*37*). It should be emphasized that adding Co-SAs/NC as a catalyst converts the reaction kinetics from first order to zero order, pointing to the intrinsic catalytic function of the Co-SAs/NC in enhancing the reaction kinetics of S reduction. Moreover, as shown in figs. S10 and S11, under high S loading (~4.5 mg cm^{-2}) and lean electrolyte (~8 μl mg^{-1}) conditions, the S reduction catalyzed by Co-SAs/NC still exhibited zero-order kinetics. This further validated the potential electrocatalytic effects of Co-SAs/NC under more practical, high-S loading conditions.

Similarly, the catalytic effects of Co-NPs/NC on the potentiostatic reduction of S were investigated by operando confocal Raman microscopy (figs. S12 and S13). The Co-NPs/NC was also able to facilitate the S conversion and also exhibited zero-order kinetics. The rate constants (k) for both Co-SAs/NC and Co-NPs/NC were derived from the slopes of their zero-order fits. As shown in Fig. 1E, the average rate constant of Co-SAs/NC was calculated to be 1.06 ± 0.20 μm^2 s^{-1}, which is much higher than that of Co-NPs/NC (0.42 ± 0.21 μm^2 s^{-1}). The deviation is mainly related to the difference between the actual active surface area and the projected area from Raman mapping due to the overlap of S clusters in the perpendicular direction to the observation plane. When normalizing the rate constant to the mass of Co, Co-SAs/NC shows a ~30 times higher k value than Co-NP$_S$/NC, pointing to the very high catalytic efficiency of SACs.

In addition to the reduction of S, the oxidation of polysulfides, catalyzed by Co-SAs/NC, was also probed via operando confocal Raman microscopy (fig. S14). The potentiostatic oxidation of Li_2S_4 was performed at a constant applied potential of 2.40 V (versus Li/Li$^+$), and the *i-t* curve is presented in fig. S14A. The operando optical images and Raman mappings are shown in figs. S15 and S14C, respectively. The region with a bandwidth of 20 cm^{-1} centered at 445 cm^{-1} (blue, intermediate-chain polysulfides; Li_2S_x, x = 3 to 5) in the Raman spectra (fig. S14B) was used to construct the Raman mappings. The gradual decrease of Li_2S_x (x = 3 to 5) during the oxidation process is shown in both the Raman spectra and the corresponding mappings. The area changes of polysulfides (Li_2S_x, x = 3 to 5) were plotted as a function of time in fig. S14D, displaying zero-order kinetics with a good linear fit (R^2 = 0.98), which was much better than the first-order fitting (R^2 = 0.84) (fig. S14E).

Different from these results, we have previously shown that the oxidation of polysulfides without any catalyst is a first-order process (*37*). The operando confocal Raman studies revealed that the Co-SAs/NC catalysts can accelerate not only the reduction of S but also the oxidation of polysulfides and change their kinetics from first order to zero order.

Concurrent galvanostatic discharge-recharge processes catalyzed by Co-SAs/NC

With the aim of investigating the catalytic function of Co-SAs/NC on the Li—S redox reactions under cell operating conditions, galvanostatic (constant current) discharge-recharge processes were studied via operando confocal Raman microscopy, monitoring the evolution of S species at the cathode in real time. The Li—S cell with an S@Co-SAs/NC cathode was discharged at 0.1 C and the voltage profile is shown in Fig. 2A. The first plateau at around 2.32 V is ascribed to the reduction of elemental S to the higher-order polysulfides, while the second plateau at around 2.1 V corresponds to the further reduction to shorter-chain polysulfides. The two plateaus in the discharge curve are consistent with the two cathodic peaks in the CV profile (fig. S5A).

The operando Raman spectra collected at different depths of discharge (DODs, %) are presented in Fig. 2B. The characteristic S peaks at 152, 219, and 473 cm^{-1} were evident at the beginning of the discharge process, subsequently decreased, and completely disappeared at around 21% DOD. Meanwhile, the peaks of long-chain polysulfides (S_x^{2-}, x = 6 to 8, 397 cm^{-1}) and intermediate-chain polysulfides (S_x^{2-}, x = 3 to 5, 450 cm^{-1}) increased gradually, and both of them reached their highest intensities at ~27% DOD, which is near the end of the first plateau. Subsequently, the peaks related to polysulfides decreased because of their further reduction into insoluble Li_2S, which has no distinct Raman signals. The long-chain polysulfides exhibited a higher rate of decrease than the intermediate-chain polysulfides. The peak intensity of the long-chain polysulfides was lower than that of intermediate-chain polysulfides after ~38% DOD, which is in the region between the first and the second plateau.

The operando morphological characterizations of S species are shown in optical images (fig. S16) and Raman mappings (Fig. 2, C and D, and movie S2). In the Raman mappings, the red, yellow, and blue colors represent S, long-chain polysulfides (S_x^{2-}, x = 6 to 8), and intermediate-chain polysulfides (S_x^{2-}, x = 3 to 5), respectively. These were constructed from the regions with a bandwidth of 20 cm^{-1} centered at 219, 398, and 450 cm^{-1}, respectively, in the Raman spectra. The evolution of S species on the surface of the cathode (*XY* plane) is presented in Fig. 2C. Within the discharge process, the initial S clusters gradually dissolved from the edges to the center and completely disappeared in the image at ~22% DOD. The polysulfides, including both long chain and intermediate chain, were formed concurrently with the dissolution of S clusters, followed by a subsequent decrease because of the further discharge, which is consistent with the Raman spectra in Fig. 2B. In addition, the

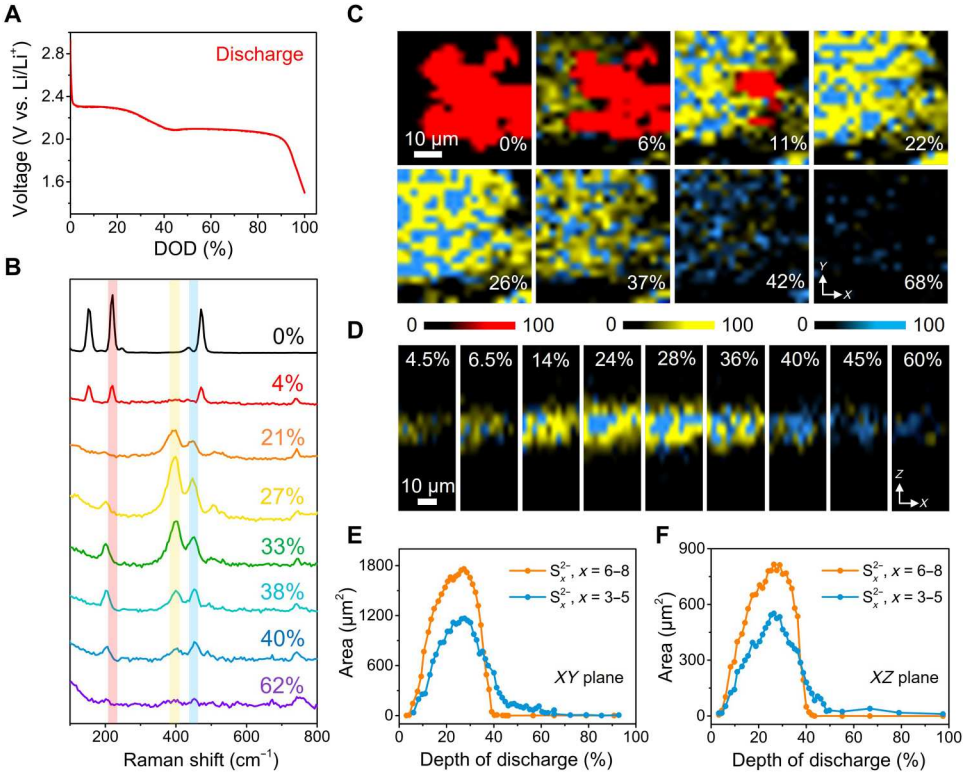

Fig. 2. Operando confocal Raman investigation of Li—S redox catalyzed by Co-SAs/NC during galvanostatic discharge process. (**A**) Voltage profile and (**B**) operando Raman spectra during the discharge process at a rate of 0.1 C (1 C = 1672 mAh g^{-1}). (**C**) Corresponding Raman mapping results in the *XY* plane. The red, yellow, and blue colors in mapping images represent S, long-chain polysulfides (S_x^{2-}, x = 6 to 8), and intermediate-chain polysulfides (S_x^{2-}, x = 3 to 5), respectively. The color contrasts remained consistent for comparison. Different DODs are indicated with %. (**D**) Corresponding Raman mappings of polysulfides in depth (*XZ* plane). Quantified area evolution of polysulfides (**E**) on surface (*XY* plane) and (**F**) in depth (*XZ* plane).

evolution of polysulfides near the cathode in the *Z* direction (*XZ* plane) was investigated by cross-sectional mappings, as presented in Fig. 2D. The generated polysulfides were anchored near the cathode and exhibited no notable diffusion to the electrolyte, in contrast to our previous observation of evident polysulfide diffusion in Li—S cells without a catalyst (*37*). This behavior is ascribed to the strong adsorption ability of Co-SAs/NC toward polysulfides. On the one hand, the MOF-derived porous carbon structures can physically confine the electrogenerated polysulfides. On the other hand, the Co single atoms can serve as polar hosts to adsorb polysulfides by chemical binding (*32*, *60*). To understand the adsorption ability of Co-SAs/NC, a combined visual adsorption experiment and UV-vis spectroscopy measurement was carried out. As shown in fig. S17, Co-SAs/NC caused fading of the brownish color of the Li_2S_6 solution and exhibited the lowest absorbance in the UV-vis spectrum, confirming the strong entrapment binding ability of Co-SAs/NC to polysulfides.

In an effort to quantitatively investigate the evolution of polysulfides, the area changes of polysulfides, calculated from Raman mappings in *XY* and *XZ* planes, were plotted as a function of DOD in Fig. 2 (E and F), respectively. In Fig. 2E, concurrent changes of long-chain and intermediate-chain polysulfides were observed. The amounts of long-chain and short-chain polysulfides increased synchronously and reached a maximum at ~28% DOD, which is in the region between the first and the second plateaus (at ~2.25 V). Subsequently, they decreased together, but the long-chain polysulfides showed a faster rate of decrease and became less evident after ~40% DOD, which is near the beginning of the second plateau in the discharge curve (Fig. 2A). The quantitative analysis of polysulfides in cross-sectional mappings (Fig. 2F) showed the same trend observed in the *XY* plane, confirming the concurrent change of long-chain and intermediate-chain polysulfides. Note that the concurrent trend of polysulfides in the discharge process, catalyzed by Co-SAs/NC, is different from the typical proposed stepwise evolution mechanism in Li—S batteries without any catalysts, where the long-chain polysulfides reach the maximum at earlier DOD than intermediate-chain polysulfides (*37*, *43*, *61*). The transformation from the stepwise mechanism to the concurrent mechanism is ascribed to the catalytic effect of Co-SAs/NC of accelerating the polysulfide transitions, which is consistent with the CV profiles in fig. S4. The same concurrent mechanism was also observed under a higher S loading (~4.5 mg cm^{-2}) and lean electrolyte (~8 μl mg^{-1}) conditions, as shown in figs. S18 to S20.

The recharge process of the Li—S cell is the reverse process of the discharge, including the oxidation of Li_2S to polysulfides, followed by the further oxidation of polysulfides to S. The Li—S cell was recharged at 0.1 C and the voltage profile is shown in fig. S21A. The selected Raman spectra, at different states of charge (SOCs), are presented in fig. S21B. During the recharge process, the peaks related to long-chain (397 cm^{-1}) and intermediate-chain (450 cm^{-1}) polysulfides exhibited consistent trends. They increased simultaneously and reached their maximum intensities at ~70% SOC, which is at the beginning of the second plateau at 2.35 V. Subsequently, they decreased together because of the oxidation of polysulfides to S. At the end of the recharge process, strong sharp signals at 152, 219, and 473 cm^{-1} were observed, which are ascribed to elemental S (S_8). The operando optical images are shown in fig. S22. The operando Raman mappings in the *XY* plane are shown in fig. S23A and movie S3, visualizing the evolution of S species on the surface of the cathode. At around 97% SOC, small S clusters were observed, because of the oxidation of polysulfides, which grew larger at the end of the recharge (100% SOC). The reformed S clusters, after the recharge process, showed considerably different sizes, shapes, and locations with respect to the initial ones at the beginning of the discharge, which indicates the "refreshing" of the S nucleation sites in the discharge-recharge cycles (*44*). The evolution of polysulfides in the *XY* plane was analyzed quantitatively in fig. S23C, which showed consistent trends for long-chain and intermediate-chain polysulfides throughout the entire recharge process, revealing "parallel" polysulfide pathways. The cross-sectional Raman mappings of polysulfides in the *Z* direction are shown in fig. S23B. The corresponding quantified area evolutions of the polysulfides are presented in fig. S23D, which exhibited the same trends of polysulfides with the results from the *XY* plane, further confirming the parallel polysulfide pathways in the recharge process.

S speciation via operando XAS

In an effort to further understand the S redox chemistry under the catalytic effect of Co-SAs/NC, operando XAS measurements of the S K-edge were performed to probe the dynamic chemical state evolution of the S composite cathode during the discharge-recharge processes. The operando coin cells were fabricated using modified CR2032 coin cell casings with a 4.5 mm diameter hole window drilled on the cap to measure scattering (Fig. 3A). To exclude the contribution of S absorption from the LiTFSI, 1.0 M lithium perchlorate ($LiClO_4$) dissolved in DOL/DME (1:1, v/v) was used as the electrolyte in all the S K-edge measurements.

Figure 3B presents x-ray absorption near-edge structure (XANES) spectra of standard references of different S species. The strong absorption peak at 2472.6 eV is the white line feature of elemental S (S_8), which is attributed to the 1s to 3p transition (*38*, *62*). Li_2S showed two peaks centered at 2473.3 and 2476.3 eV, respectively. The latter peak is identified as a constructive interference feature, which is apparently different from the destructive interference feature of elemental S (S_8) at ~2476 eV (*63*). The spectra of polysulfides were characterized by two peaks. One is the main-edge feature at the same energy as elemental S (2472.6 eV), which likely arises from the "internal" S atoms in the polysulfide chains. The other one is the lower energy edge feature near 2470.8 eV, corresponding to the charged "terminal" S atoms at either end of the polysulfide chain dianions (*40*, *64*). Closely monitoring the near-edge features of polysulfides with different chain lengths, when shortening the polysulfide chain, the intensity of the main-edge peak decreased, while the intensity of the lower energy edge peak increased because of the increasing ratio of terminal S atoms to all the S atoms in a polysulfide chain. This observation is also consistent with reported first-principles simulation results (*65*, *66*).

Figure 3C displays operando XANES spectra obtained throughout the first discharge-recharge cycle at 0.1 C in a Li—S cell with an S@Co-SAs/NC cathode. As presented in Fig. 3D, the distinct features evolving through the cycle are shown by the selected spectra from Fig. 3C. At the initial state, the spectrum exhibited one strong absorption (peak A) at 2472.6 eV, corresponding to the elemental S (S_8) in the cathode. Within the discharge process, the intensity of peak A decreased while the peak B at 2470.8 eV increased, representing the conversion of elemental S into polysulfides. Subsequently, the intensity of peak B decreased because of the further reduction of polysulfides to Li_2S. The Li_2S signal, characterized by

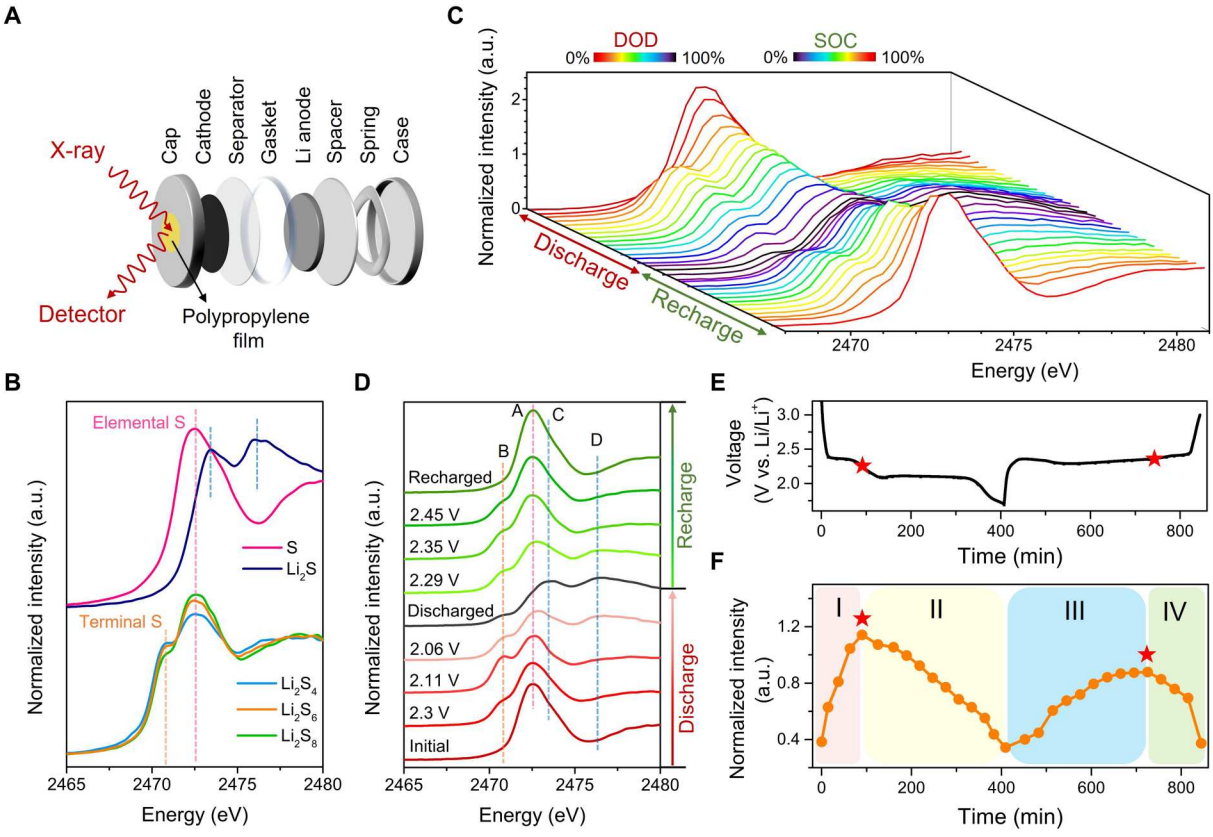

Fig. 3. Operando S K-edge XANES analysis of S speciation under the catalytic effects of Co-SAs/NC. (**A**) Schematic of an operando coin cell. (**B**) Normalized S K-edge XANES spectra of standard references: S, Li_2S, and polysulfide solutions (Li_2S_4, Li_2S_6, and Li_2S_8). (**C**) Evolution of S K-edge XANES spectra during a full galvanostatic cycle. (**D**) XANES spectra selected from specific points during the cycling, labeled by the voltage. (**E**) Voltage profile measured at 0.1 C and (**F**) the corresponding evolution of the intensity of peak B (2470.9 eV; representing LiPSs) during cycling. a.u., arbitrary units.

peak C (2473.3 eV) and peak D (2476.3 eV), became evident at the end of the discharge process. In the subsequent recharge process, the formed Li_2S was oxidized to polysulfides, as shown by the decreasing intensity of peaks C and D as well as the increasing intensity of the peak B. At the end of the recharge process, the spectrum showed an intense peak A without the feature of peak B, indicating the reformation of elemental S.

To further reveal the changes of polysulfides during the cycling, the voltage profile and the normalized intensity changes of peak B are presented in Fig. 3 (E and F), respectively, correlating the electrochemical and XAS features. During the discharge process, the intensity of peak B increased and reached a maximum at ~2.25 V, which is in the region between the two discharge plateaus, in agreement with our operando Raman results (Fig. 2). Subsequently, the intensity decreased monotonically until the end of discharge, suggesting the continuous consumption of polysulfides. In the recharge process, the intensity of peak B increased along with the first charge plateau and reached a maximum at ~2.35 V, after which it decreased because of the oxidation of polysulfides to elemental S, in agreement with the Raman analysis (fig. S23).

In addition to the operando study of Li—S cells with Co-SAs/NC catalysts, we performed the same experiments for Li—S cells without any catalyst. The operando XANES spectra and the intensity evolution of peak B are shown in fig. S24. During the discharge process, the maximum of peak B appeared at the beginning of the second plateau. In the subsequent discharging, the peak intensity decreased slowly at first (indicated by region II-a), followed by a decrease with a larger slope (indicated by region II-b). These observations are consistent with reported studies (*38*, *39*) and are in accordance with the electrochemical features of the typical stepwise mechanism for polysulfide transitions. However, in contrast to this "two-step" decrease of polysulfides in the discharge process, Li—S cells catalyzed by Co-SAs/NC showed a different trend with a near linear decrease in region II (Fig. 3F), which was reproducible in different cycles and different cells (fig. S25). This "near linear decrease" feature may be related to, at least in part, the concurrent change of long-chain and intermediate-chain polysulfides in the discharge process because of the accelerated kinetics under the catalytic effects of Co-SAs/NC, as indicated by the operando Raman results (Fig. 2).

Evolution of Co-SAs/NC via operando XAS

After investigating the S speciation under the catalytic effects of Co-SAs/NC during the redox processes, XAS measurements of the Co K-edge were carried out to assess the electronic structure and local environment of the Co atoms in Co-SAs/NC and to observe the dynamic evolution of active sites directly under catalytic conditions. Figure 4A presents the normalized Co K-edge XANES spectra of Co-SAs/NC, along with the data for Co foil, CoO, and CoS_2 as references. The spectrum of Co-SAs/NC exhibited a weak pre-edge feature at 7709 eV, arising from the 1s → 3d transition, which is a

fingerprint of the centrosymmetric square planar Co—N_x structure (*67*–*69*). The main-edge absorption was attributed to an electronic transition from 1s to 4p orbitals. As presented in fig. S26A, the absorption edge of Co-SAs/NC (7720 eV) was close to that of the CoO reference (7721 eV), indicating that the oxidation state of Co in Co-SAs/NC was around +2, which is consistent with the XPS results (fig. S3). The corresponding Fourier-transformed (FT) k^3-weighted extended x-ray absorption fine structure (EXAFS) profiles in R space (without phase correction) are shown in Fig. 4B. Only one prominent signal of Co-SAs/NC was observed at 1.41 Å, corresponding to Co—N scattering in the first shell, which is shorter than the Co—O path (1.71 Å) in CoO and the Co—S path (1.89 Å) in CoS_2. In addition, the Co—Co path at 2.18 Å (Co foil) and other high-shell signals were almost undetectable in Co-SAs/NC, validating the single-atom nature of the Co sites, which is in agreement with the HAADF-STEM images (fig. S2). The first-shell EXAFS fitting of Co-SAs/NC was performed following the Co—N scattering path, as shown in R space (Fig. 4C) and *k* space (fig. S27). The fitted curves were well-matched to the experimental data. As presented in table S1, the fitted coordination number of Co—N was 3.91 and the mean bond length was 1.90 Å. Together with the pre-edge features in the XANES spectrum, the local square planar Co—N_4 structure of Co atoms in Co-SAs/NC was ascertained, as shown in the inset of Fig. 4C.

Operando XAS measurements of the Co K-edge were performed to detect the dynamic changes of electronic structure and local environment of the Co sites in Co-SAs/NC under different applied potentials and, thus, provide complementary information on the catalytic effects of Co-SAs/NC in Li—S batteries. The operando-normalized Co K-edge XANES spectra at different discharge states are presented in Fig. 4D, displaying a potential-dependent shift of the rising edge region. As shown in the magnified inset of Fig. 4D, when

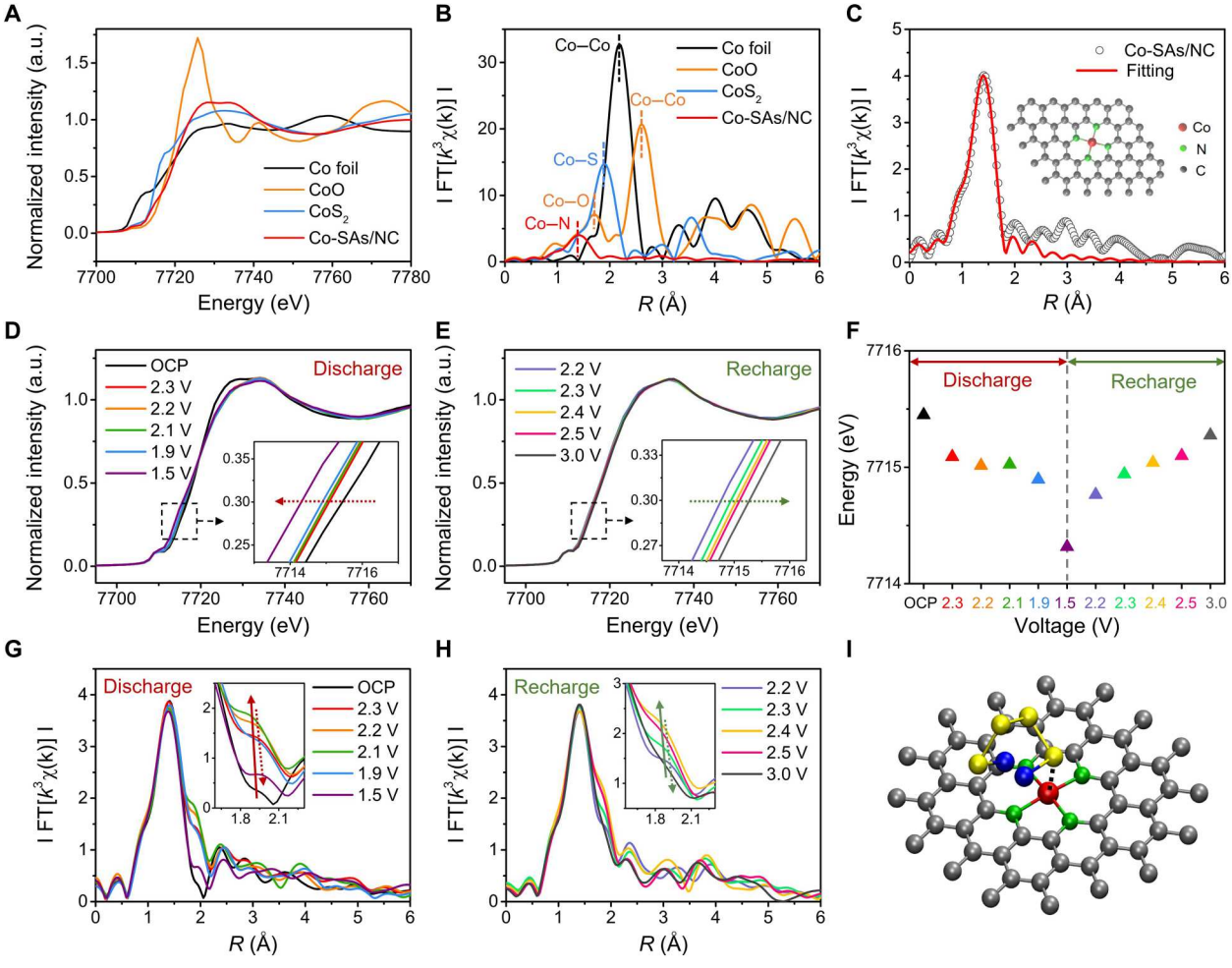

Fig. 4. Operando Co K-edge XAS analysis of the dynamic evolution of Co single-atom sites. (**A**) Normalized Co K-edge XANES and (**B**) k^3-weighted FT-EXAFS spectra of Co-SAs/NC and Co references: Co foil, CoO, and CoS_2, shown in ($R + \Delta$) distances, without phase correction. (**C**) Corresponding Co K-edge k^3-weighted FT-EXAFS fitting curves of Co-SAs/NC in R space. The inset is the schematic structure of Co-SAs/NC. Operando-normalized Co K-edge XANES spectra of Co-SAs/NC (**D**) discharged and (**E**) recharged to different electrochemical states in a Li—S battery. Insets are the magnified pre-edge regions. (**F**) Evolution of the pre-edge absorption energy, indicated in the insets of (D) and (E), as a function of the discharge and recharge states. Operando k^3-weighted FT-EXAFS spectra of Co-SAs/NC (**G**) discharged and (**H**) recharged to different electrochemical states in a Li—S battery. Insets are the magnified shoulder peak regions. The arrows with solid and dashed lines indicate the gradual increase and decrease processes of the shoulder peak, respectively. (**I**) Schematic illustration of the Co—S coordination bond between a Co single-atom site and a S atom from a polysulfide molecule (Li_2S_4). Red (Co), green (N), gray (C), yellow (S), and blue (Li).

the voltage decreased from open circuit potential (OCP; ~3.0 V) to 2.3, 2.2, 2.1, 1.9, and finally 1.5 V following the discharge process, the XANES spectra shifted gradually to a lower-energy region by >0.1 eV. The downshift of energy indicates a decrease in the oxidation state of Co, accompanied by the reduction from elemental S to polysulfides, and then to Li_2S. In the subsequent recharge process (Fig. 4E), with increasing applied potentials, the XANES spectra shifted back to higher energies, indicating an increase in the oxidation state of Co, corresponding to the oxidation of S species back to elemental S. The evolution of energy in the rising edge region at the same normalized intensity, indicated by dashed arrows in the insets of Fig. 4 (D and E), is presented as a function of discharge and recharge states (Fig. 4F). The energy changes throughout the discharge-recharge process demonstrated a similar shape to the typical discharge-recharge voltage profiles, which presumably reflects the interactions between the Co single-atom sites and different S species.

Operando EXAFS spectra in R space collected at different states during discharge and recharge processes are presented in Fig. 4 (G and H), respectively. In the discharge process, there was no evidence of changes observed for the Co—N shell at 1.41 Å, while a shoulder peak appeared at around 1.9 Å, which was ascribed to Co—S interactions. As shown in the inset of Fig. 4G, at the beginning of the discharge, the signal for the Co—S coordination bond was weak. Subsequently, the magnitude of the Co—S peak increased within the reduction process from elemental S to polysulfides. The intensity of the Co—S peak reached a maximum at 2.1 V, which could be related to the strong interaction between Co and polysulfides. Afterward, the amplitude of the Co—S shell decreased gradually with the further reduction of polysulfides to Li_2S. These observations indicated that the Co—S interactions were mainly due to the coordination between the S atoms from polysulfides and the single-atom Co sites, as illustrated in Fig. 4I. In the recharge process, a similar evolution of the Co—S coordination bonds was observed. The initial increment of the Co—S peak corresponded to the generation of polysulfides from Li_2S, and the subsequent decrease in magnitude was due to the further oxidation of polysulfides back to elemental S. The operando EXAFS results revealed the evolution of Co—S coordination bonds in the discharge-recharge processes and suggested that polysulfides can coordinate to Co atoms more strongly, compared to elemental S and Li_2S.

Co-SAs/NC catalyzed Li—S redox mechanism

With the combination of the operando confocal Raman studies and the operando XAS analyses, the mechanistic details of Li—S redox under the catalytic effect of Co-SAs/NC were explored. Figure 5A presents the potentiostatic reduction process of the S cluster. The S cluster at different states of reduction (SOR, %) is represented by different colors. In the reduction process, the S clusters dissolve from the edge to the center. In the absence of a catalyst, the consumption rate of S slows down with a decreasing active area of S, which follows first-order kinetics (Fig. 5B) (*37*). In contrast, the Co-SAs/NC changes the reduction of S from first-order to zero-order kinetics, with a constant reaction rate that is not influenced by changes in the active amount of S (Fig. 5C), according to our operando confocal Raman results (Fig. 1). This points to the catalytic effects of Co-SAs/NC on the S reduction reaction, enhancing the kinetics of this solid-liquid transition.

The discharge processes of Li—S batteries without any catalyst and with Co-SAs/NC catalysts are schematically illustrated in Fig. 5 (D and G), respectively. Typically, the evolution of S species in Li—S batteries follows the following sequence: S (S_8) → long-chain polysulfides (S_x^{2-}, x = 6 to 8) → intermediate-chain polysulfides (S_x^{2-}, x = 3 to 5) → Li_2S_2/Li_2S. Large amounts of long-chain polysulfides are formed initially, followed by the accumulation of intermediate-chain polysulfides. As presented in Fig. 5E, the amount of long-chain polysulfides increases and reaches its maximum first, due to the reduction of elemental S. Afterward, the decrease is attributed to the liquid-liquid transition from long-chain polysulfides to intermediate-chain polysulfides, accompanied by an increase in the amount of intermediate-chain polysulfides. The maximum of the intermediate-chain polysulfides lags behind the maximum of the long-chain polysulfides. Such nonsynchronous changes are features of the stepwise mechanism of the multistep polysulfide transitions. However, under the catalytic effects of Co-SAs/NC, the long-chain and intermediate-chain polysulfides exhibit concurrent trends. The maximum of intermediate-chain polysulfides exists at the same DOD with the long-chain polysulfides (Fig. 5H), based on the operando Raman quantitative analysis in Fig. 2. Note that, in the concurrent mechanism, the evolution of S species still follows the same sequence as in the stepwise mechanism. The accelerated reaction kinetics for the multistep conversions, due to electrocatalysis, is the major reason leading to the experimentally observed concurrent evolution of polysulfides. On the one hand, the concurrent increase of intermediate-chain polysulfides with long-chain polysulfides indicates the accelerated kinetics of the liquid-liquid polysulfide transition from long chain to intermediate chain. One the other hand, after the maximum point of the polysulfides, although the long-chain polysulfides are reduced to intermediate-chain polysulfides, the latter does not accumulate. This can be ascribed to the fast consumption of intermediate-chain polysulfides by the further reduction to Li_2S, suggesting the facilitated kinetics of the liquid-solid phase transition process. The faster reaction kinetics facilitates the conversion of S species efficiently and can contribute to a higher capacity (fig. S6A).

The evolution of polysulfides, indicated by the lower energy edge feature (peak B) in the XAS spectra of the S K-edge (Fig. 3 and fig. S24), are schematically illustrated in Fig. 5 (F and I), representing the situation without catalyst and with Co-SAs/NC, respectively. In the absence of catalyst, the evolution of the polysulfide signal presents an initial increase (region I), followed by a decrease, which can be further divided into two regions (region II-a and region II-b). The relatively mild change in region II-a corresponds to the region in between the orange and blue dashed lines in Fig. 5E, where the long-chain polysulfides decrease while the intermediate-chain polysulfides increase and, thus, the total change of polysulfides in the system is not marked. The subsequent faster decrease in region II-b is attributed to the further reduction to Li_2S. By comparison, in the presence of Co-SA, the evolution of the polysulfide feature exhibits only one decrease region (II) with a near linear decrease, which is consistent with the concurrent decrease of the long-chain and intermediate-chain polysulfides in Fig. 5H. The operando XAS and Raman results validate the different mechanisms of polysulfide conversions with and without Co-SAs/NC catalysts, unequivocally revealing the catalytic effects of Co-SAs/NC on Li—S redox reactions.

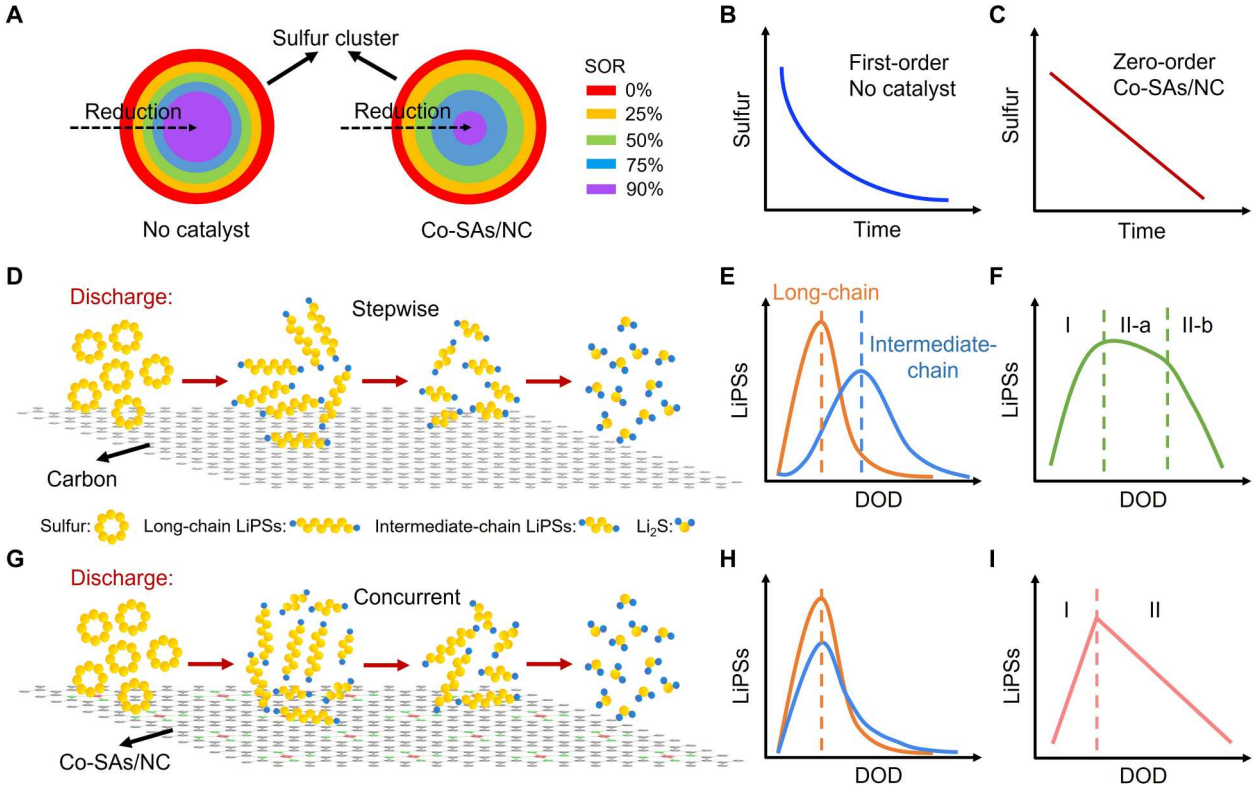

Fig. 5. Mechanistic comparison of Li—S redox reactions at a S cathode with and without Co-SAs/NC. (**A**) Schematic of active surface area evolution of a S cluster during the potentiostatic reduction process without any catalysts (left) and under the catalytic effects of Co-SAs/NC (right). The color bars indicate different SOR (%), taking the reduction of the S cluster on Co-SAs/NC as the reference. Plot of the area changes of S clusters as a function time (**B**) without any catalyst and (**C**) under the catalytic effect of Co-SAs/NC. Schematic illustrations of the discharge process (**D**) without any catalyst and (**G**) under the catalytic effects of Co-SAs/NC. Evolution of long-chain polysulfides (orange; S_x^{2-}, $x = 6$ to 8) and intermediate-chain polysulfides (blue; S_x^{2-}, $x = 3$ to 5) during the discharge process (**E**) without any catalyst and (**H**) under the catalytic effects of Co-SAs/NC, based on operando confocal Raman results. Evolution of polysulfides in the discharge process (**F**) without any catalyst and (**I**) under the catalytic effects of Co-SAs/NC, based on operando XAS results.

In addition, first-principles calculations based on density functional theory (DFT) were carried out to assess the Gibbs free energies for S redox reactions under conditions with and without Co-SAs/NC, respectively. The calculated Gibbs free energy profiles are presented in fig. S28. The energy barriers of both the long-intermediate polysulfide transition ($Li_2S_8 \rightarrow Li_2S_6 \rightarrow Li_2S_4$) and the intermediate-short transition ($Li_2S_4 \rightarrow Li_2S_2 \rightarrow Li_2S$) on Co-SAs/NC were lower, compared to the case without catalyst. The calculated results are consistent with our experimental data and indicate that the multistep polysulfide conversions are more favorable on a Co-SAs/NC surface/substrate.

In summary, we have monitored the real-time evolution of S species and the dynamic changes of Co single-atom catalytic sites in Li—S batteries via operando confocal microscopy and operando XAS, which have provided new insights into the reaction kinetics and catalytic mechanisms of the multistep Li—S redox reactions. On the basis of the potentiostatic reduction/oxidation studies, we have found that Co-SAs/NC catalysts are able to facilitate the kinetics of S reduction and polysulfide oxidation as well as change their original first-order reaction kinetics to zero-order kinetics. Moreover, during the galvanostatic discharge process without catalysts, the evolution of different polysulfides followed a stepwise mechanism with nonsynchronous changes of the long-chain and intermediate-chain polysulfides. In contrast, with Co-SAs/NC catalysts, the long-chain and intermediate-chain polysulfides exhibited concurrent trends, indicating the accelerated kinetics of liquid-liquid polysulfide conversion and liquid-solid phase transition under the catalytic effects of Co-SAs/NC. In addition, the dynamic electronic and structural changes of the catalytic Co sites were captured via operando XAS of the Co K-edge, suggesting the formation of Co—S coordination bonds during electrocatalysis. Operando confocal Raman and XAS studies have provided compelling evidence of the S speciation and have enabled a comprehensive understanding of the underlying kinetics and mechanisms of Li—S redox processes catalyzed by Co-SAs/NC. These results and approaches can provide promising insights into the in-depth understanding of the reaction mechanisms in Li—S batteries and spark new inspirations of systematically deciphering complex pathways in other sustainable electrical energy storage systems.

MATERIALS AND METHODS

Synthesis of the catalysts

ZIF-67 and ZIF-8 were used as the carbon precursors (ZIF, zeolitic imidazolate frameworks). ZIF-67 is composed of a Co center

coordinated by four imidazolate groups, while ZIF-8 has zinc as the metal center. Typically, a mixture of $Co(NO_3)_2{\cdot}6H_2O$ and $Zn(NO_3)_2{\cdot}6H_2O$ with different molar ratios of Co^{2+}/Zn^{2+} was dissolved in a mixed solvent of 40 ml of ethanol and 40 ml of methanol, where the total molar amounts of Zn^{2+} and Co^{2+} were 6 mmol with stoichiometric numbers represented by x and y in moles. Another mixture of 2-methylimidazole (1.97 g; Sigma-Aldrich) and 1-methylimidazole (0.49 g; Sigma-Aldrich) with 40 ml of methanol and 40 ml of ethanol was then added under magnetic stirring. The solution was left standing still for 48 hours at room temperature. The formed precipitate was collected by centrifugation, washed with methanol, and dried in an oven at 60°C. The product is denoted as MOF-Zn_xCo_y. The as-synthesized MOF-Zn_xCo_y particles were transferred into a flow furnace and heated to 300°C for 1.5 hours and then 900°C for 2 hours in flowing forming gas (5% H_2 + 95% N_2). The catalysts were collected after the furnace was turned off and cooled down. The desired Co-SAs/NC, Co-NPs/NC, and NC composites were obtained by pyrolyzing MOF-Zn_xCo_y with x/y ratio of 20:1, 0:1, and 1:0, respectively. The Co loading in the as-prepared Co-SAs/NC was around 1.6 wt %, measured by inductively coupled plasma optical emission spectroscopy (ICP-OES).

Preparation of the S cathodes

S was loaded into the above catalyst composites by a melt-diffusion method. A mixture of 70 wt % S and 30 wt % catalyst was first ball-milled for 20 min, followed by melt-diffusion at 155°C for 12 hours in an oven. The slurry of S@catalyst composite, Super P (Alfa-Aesar, 99%), and polyvinylidene fluoride (PVDF) with a mass ratio of 8:1:1 in *N*-methyl-2-pyrrolidinone (anhydrous, 99.5%; Sigma-Aldrich) were bladed onto carbon paper (AvCarb EP40, Fuelcell Store; 0.19 mm thickness) and dried overnight at 60°C. The S loading of cathode was 1.5 to 2 mg cm^{-2} if not otherwise specified.

Materials characterizations

Crystal structures were confirmed by powder XRD using a Rigaku Ultima VI diffractometer, measured from 20° to 80° at a scan rate of 4° min^{-1}. The metal loading of Co was measured by ICP-OES (SPECTRO ARCOS FHE12). XPS spectra were collected in a Surface Science Instruments SSX-100 operated under a working pressure at 2×10^{-9} torr. For STEM and EELS analyses, the sample was prepared by drop-casting Co-SAs/NC ethanol dispersions on lacey carbon on Cu TEM grids and baked out at 130°C for 5 hours to remove contaminants before STEM-EELS characterization. The STEM imaging with EELS elemental mapping was acquired on a fifth-order aberration-corrected FEI Titan Themis operated at 120 keV. Beam damage of the sample was routinely examined before and after EELS mapping. The STEM images were processed by ImageJ software, and all the elemental maps were processed with principal components analysis with three components and a linear combination of power law for background subtraction.

Electrochemical measurements

Electrochemical performance was evaluated using CR2032 coin cell casings, which were assembled in an argon-filled glove box with oxygen and water contents below 0.1 parts per million. A Celgard 2300 polypropylene separator was used to separate the S cathode and Li metal anode. The electrolyte was 1.0 M LiTFSI dissolved in a mixed solvent of DOL and DME (1:1, v/v) with 2 wt % $LiNO_3$ as an additive. Galvanostatic discharge/charge measurements were performed with a Neware battery test station over the voltage range of 1.8 to 2.8 V (versus Li^+/Li). CV was conducted on a Bio-Logic SP-150 potentiostat, and EIS tests were carried out from 0.1 Hz to 100 kHz on the same workstation. The tests were carried out at 25° ± 1°C. The symmetric coin cell was assembled for CV measurements to probe the polysulfide conversion kinetics. Symmetric cells were assembled with two electrodes that consisted of a mixture of 80 wt % of the catalyst (Co-SAs/NC, Co-NPs/NC, and NC) and 20 wt % of PVDF. The electrolyte was 0.5 M Li_2S_6 and 1.0 M LiTFSI in a mixed solvent of DOL and DME (1:1, v/v). CV was performed between −1.4 and 1.4 V at a scan rate of 2 mV s^{-1}.

Operando confocal Raman microscopy characterization

The operando cell was adapted from the CR2032 coin cell with a 3-mm diameter glass window (0.13- to 0.17-mm thickness; Fisherbrand). For the potentiostatic reduction of S and galvanostatic discharge-recharge experiments, S cathodes (S@catalyst) were prepared by coating a slurry of S:PVDF (7:2) onto the pinhole-modified carbon paper, followed by an additional layer of catalyst:PVDF (8:2) onto the dried S layer. For the experiments of oxidation of polysulfides, cathodes were prepared by coating a slurry of catalyst:PVDF (8:2) onto the pinhole-modified carbon paper. The Raman spectra and mapping images were obtained via a WITec Alpha300R confocal Raman microscope. The calibration of the spectra and color contrast of the images were set consistently for quantification and comparison using the software of Project Five 5.1. The 20 cm^{-1} regions centered around the peak positions on the spectra were selected for mapping. Areas in the Raman mapping were extracted and quantified by ImageJ. For S clusters, projected areas were mapped, which served as proxy for the active surface areas. For Li_2S_4 catholytes (0.8 M), the areas at the open circuit were treated as pristine concentrations. Because the Li_2S_4 catholytes are homogeneous solutions, the changes of the areas from Raman mapping were assumed to be proportional to changes in concentration. Operando characterizations for potentiostatic and galvanostatic measurements were achieved by controlling the voltage/current rate of the cells and monitoring the current-time/voltage-time responses, respectively, with a potentiostat (Metrohm Autolab PGSTAT302N).

Operando XAS characterization

Operando S K-edge XAS spectra were collected at the TES beamline (8-BM) of the National Synchrotron Light Source II. All of the operando experiments were carried out under constant helium flow in the sample chamber, and the data were collected in fluorescence mode. The operando cell was adapted from a CR2032 coin cell using a polypropylene window (diameter: 4.5 mm). The electrolyte was 1 M $LiClO_4$ in DOL/DME (1:1, v/v) with 2 wt % $LiNO_3$. Co K-edge XAS spectra were acquired at the PIPOXS beamline of the Cornell High Energy Synchrotron Source under ring conditions of 100 mA at 6 GeV. Ex situ powder samples (Co-SAs/NC, Co-NPs/NC, and Co references) were measured under transmission mode. Operando XAS measurements were carried out in fluorescence mode. The operando cell was adapted from a CR2032 coin cell using a Kapton window (diameter: 6 mm). The electrolyte was 1 M LiTFSI in DOL/DME (1:1, v/v). XAS spectra of Co were acquired from 7550 to 8350 eV using a Si(111) monochromator, with a beam spot size of 0.72 mm by 0.72 mm and averaged from

around 25 spectra using a four-element Vortex detector to enhance the signal-to-noise ratio. All XAS spectra were normalized and analyzed using Athena and Artemis software packages (*70*).

Theoretical calculations

DFT calculations were preformed using the ORCA 5.0 computational package (*71*). The models of graphene flakes, Co-SAs/NC, and LiPSs were constructed in Avogadro molecular editor (*72*). Before geometry optimization, we generated the initial coordinates of the species via Packmol (*73*). For each LiPS and catalyst pair, we conducted the calculation with at least 10 different initial configurations to find the optimal total SCF energy. Because the catalysts include Co atoms, we applied unrestricted Kohn-Sham DFT to account for the open-shell system. The PBEh-3c functional was used to compute the optimized geometries, energies, and orbitals. The def2-mSVP basis and the auxiliary def 2/J basis were implemented. The RIJCOSX approximation was used to accelerate Hartree-Fock and hybrid DFT calculations. The data of orbitals were output as Gaussian cube files and visualized through visual molecular dynamics (VMD), where the density functions of electron orbitals were plotted (*74*). The energy profiles and corresponding optimized geometries are shown in fig. S28 and figs. S29 and S30, respectively. Compared to previous research (*31*, *32*), our model was focused on calculating the interaction between a single molecule and a large graphene substrate. Instead of using periodic boundary condition, this approach can exclude the interference between the LiPSs and their mirror molecules in the simulation.

Supplementary Materials

This PDF file includes:
Figs. S1 to S30
Table S1
References

Other Supplementary Material for this manuscript includes the following:
Movies S1 to S3

REFERENCES AND NOTES

1. Y. Sun, N. Liu, Y. Cui, Promises and challenges of nanomaterials for lithium-based rechargeable batteries. *Nat. Energy* **1**, 16071 (2016).
2. B. Dunn, H. Kamath, J. M. Tarascon, Electrical energy storage for the grid: A battery of choices. *Science* **334**, 928–935 (2011).
3. Y. X. Yin, S. Xin, Y. G. Guo, L. J. Wan, Lithium-sulfur batteries: Electrochemistry, materials, and prospects. *Angew. Chem. Int. Ed.* **52**, 13186–13200 (2013).
4. H. J. Peng, J. Q. Huang, X. B. Cheng, Q. Zhang, Review on high-loading and high-energy lithium–sulfur batteries. *Adv. Energy Mater.* **7**, 1700260 (2017).
5. M. R. Busche, P. Adelhelm, H. Sommer, H. Schneider, K. Leitner, J. Janek, Systematical electrochemical study on the parasitic shuttle-effect in lithium-sulfur-cells at different temperatures and different rates. *J. Power Sources* **259**, 289–299 (2014).
6. S.-Y. Lang, R.-J. Xiao, L. Gu, Y.-G. Guo, R. Wen, L.-J. Wan, Interfacial mechanism in lithium−sulfur batteries: How salts mediate the structure evolution and dynamics. *J. Am. Chem. Soc.* **140**, 8147–8155 (2018).
7. P. G. Bruce, S. A. Freunberger, L. J. Hardwick, J. M. Tarascon, Li-O_2 and Li-S batteries with high energy storage. *Nat. Mater.* **11**, 19–29 (2012).
8. X. Ji, K. T. Lee, L. F. Nazar, A highly ordered nanostructured carbon–sulphur cathode for lithium–sulphur batteries. *Nat. Mater.* **8**, 500–506 (2009).
9. N. Zhang, Y. Yang, X. Feng, S. H. Yu, J. Seok, D. A. Muller, H. D. Abruña, Sulfur encapsulation by MOF-derived CoS_2 embedded in carbon hosts for high-performance Li-S batteries. *J. Mater. Chem. A* **7**, 21128–21139 (2019).
10. J. Zheng, J. Tian, D. Wu, M. Gu, W. Xu, C. Wang, F. Gao, M. H. Engelhard, J. G. Zhang, J. Liu, J. Xiao, Lewis acid-base interactions between polysulfides and metal organic framework in lithium sulfur batteries. *Nano Lett.* **14**, 2345–2352 (2014).
11. X. Tao, J. Wang, Z. Ying, Q. Cai, G. Zheng, Y. Gan, H. Huang, Y. Xia, C. Liang, W. Zhang, Y. Cui, Strong sulfur binding with conducting Magnéli-phase Ti_nO_{2n-1} nanomaterials for improving lithium-sulfur batteries. *Nano Lett.* **14**, 5288–5294 (2014).
12. X. Liang, C. Hart, Q. Pang, A. Garsuch, T. Weiss, L. F. Nazar, A highly efficient polysulfide mediator for lithium-sulfur batteries. *Nat. Commun.* **6**, 5682 (2015).
13. J. Zhang, Z. Li, X. W. D. Lou, A freestanding selenium disulfide cathode based on cobalt disulfide-decorated multichannel carbon fibers with enhanced lithium storage performance. *Angew. Chem. Int. Ed.* **56**, 14107–14112 (2017).
14. G. Zhou, H. Tian, Y. Jin, X. Tao, B. Liu, R. Zhang, Z. W. Seh, D. Zhuo, Y. Liu, J. Sun, J. Zhao, C. Zu, D. S. Wu, Q. Zhang, Y. Cui, Catalytic oxidation of Li_2S on the surface of metal sulfides for Li-S batteries. *Proc. Natl. Acad. Sci. U.S.A.* **114**, 840–845 (2017).
15. D. Su, M. Cortie, G. Wang, Fabrication of N-doped graphene–carbon nanotube hybrids from prussian blue for lithium–sulfur batteries. *Adv. Energy Mater.* **7**, 1602014 (2017).
16. W. Li, H. Yao, K. Yan, G. Zheng, Z. Liang, Y. M. Chiang, Y. Cui, The synergetic effect of lithium polysulfide and lithium nitrate to prevent lithium dendrite growth. *Nat. Commun.* **6**, 7436 (2015).
17. S. S. Zhang, Role of $LiNO_3$ in rechargeable lithium/sulfur battery. *Electrochim. Acta* **70**, 344–348 (2012).
18. M. Yu, S. Zhou, Z. Wang, Y. Wang, N. Zhang, S. Wang, J. Zhao, J. Qiu, Accelerating polysulfide redox conversion on bifunctional electrocatalytic electrode for stable Li-S batteries. *Energy Stor. Mater.* **20**, 98–107 (2019).
19. H. Al Salem, G. Babu, C. V. Rao, L. M. R. Arava, Electrocatalytic polysulfide traps for controlling redox shuttle process of Li-S batteries. *J. Am. Chem. Soc.* **137**, 11542–11545 (2015).
20. A. H. Shao, Z. Zhang, D. G. Xiong, J. Yu, J. X. Cai, Z. Y. Yang, Facile synthesis of a "two-in-one" sulfur host featuring metallic-cobalt-embedded N-doped carbon nanotubes for efficient lithium-sulfur batteries. *ACS Appl. Mater. Interfaces* **12**, 5968–5978 (2020).
21. W. Wang, Y. Zhao, Y. Zhang, J. Wang, G. Cui, M. Li, Z. Bakenov, X. Wang, Defect-rich multishelled Fe-doped Co_3O_4 hollow microspheres with multiple spatial confinements to facilitate catalytic conversion of polysulfides for high-performance Li-S batteries. *ACS Appl. Mater. Interfaces* **12**, 12763–12773 (2020).
22. Y. Zheng, Y. Yi, M. Fan, H. Liu, X. Li, R. Zhang, M. Li, Z.-A. Qiao, A high-entropy metal oxide as chemical anchor of polysulfide for lithium-sulfur batteries. *Energy Stor. Mater.* **23**, 678–683 (2019).
23. J. Yu, J. Xiao, A. Li, Z. Yang, L. Zeng, Q. Zhang, Y. Zhu, L. Guo, Enhanced multiple anchoring and catalytic conversion of polysulfides by amorphous MoS_3 nanoboxes for high-performance Li-S batteries. *Angew. Chem. Int. Ed.* **59**, 13071–13078 (2020).
24. D.-R. Deng, T.-H. An, Y.-J. Li, Q.-H. Wu, M.-S. Zheng, Q.-F. Dong, Hollow porous titanium nitride tubes as a cathode electrode for extremely stable Li–S batteries. *J. Mater. Chem. A* **4**, 16184–16190 (2016).
25. T. Tan, N. Chen, Z. Wang, Z. Tang, H. Zhang, Q. Lai, Y. Liang, Thorn-like carbon nanofibers combined with molybdenum nitride nanosheets as a modified separator coating: an efficient chemical anchor and catalyst for Li-S batteries. *ACS Appl. Energy Mater.* **5**, 6654–6662 (2022).
26. J. Song, T. Xu, M. L. Gordin, P. Zhu, D. Lv, Y. B. Jiang, Y. Chen, Y. Duan, D. Wang, Nitrogen-doped mesoporous carbon promoted chemical adsorption of sulfur and fabrication of high-areal-capacity sulfur cathode with exceptional cycling stability for lithium-sulfur batteries. *Adv. Funct. Mater.* **24**, 1243–1250 (2014).
27. Q. Pang, J. Tang, H. Huang, X. Liang, C. Hart, K. C. Tam, L. F. Nazar, A nitrogen and sulfur dual-doped carbon derived from polyrhodanine@cellulose for advanced lithium–sulfur batteries. *Adv. Mater.* **27**, 6021–6028 (2015).
28. Y. Qiu, W. Li, W. Zhao, G. Li, Y. Hou, M. Liu, L. Zhou, F. Ye, H. Li, Z. Wei, S. Yang, W. Duan, Y. Ye, J. Guo, Y. Zhang, High-rate, ultralong cycle-life lithium/sulfur batteries enabled by nitrogen-doped graphene. *Nano Lett.* **14**, 4821–4827 (2014).
29. X. F. Yang, A. Wang, B. Qiao, J. Li, J. Liu, T. Zhang, Single-atom catalysts: A new frontier in heterogeneous catalysis. *Acc. Chem. Res.* **46**, 1740–1748 (2013).
30. A. Wang, J. Li, T. Zhang, Heterogeneous single-atom catalysis. *Nat. Rev. Chem.* **2**, 65–81 (2018).
31. C. Zhao, G.-L. Xu, Z. Yu, L. Zhang, I. Hwang, Y.-X. Mo, Y. Ren, L. Cheng, C.-J. Sun, Y. Ren, X. Zuo, J.-T. Li, S.-G. Sun, K. Amine, T. Zhao, A high-energy and long-cycling lithium–sulfur pouch cell via a macroporous catalytic cathode with double-end binding sites. *Nat. Nanotechnol.* **16**, 166–173 (2020).
32. Z. Du, X. Chen, W. Hu, C. Chuang, S. Xie, A. Hu, W. Yan, X. Kong, X. Wu, H. Ji, L.-J. Wan, Cobalt in nitrogen-doped graphene as single-atom catalyst for high-sulfur content lithium-sulfur batteries. *J. Am. Chem. Soc.* **141**, 3977–3985 (2019).

33. Y. Li, Y. Zeng, Y. Chen, D. Luan, S. Gao, X. Wen Lou, Mesoporous N-rich carbon with single-Ni atoms as a multifunctional sulfur host for Li-S batteries. *Angew. Chem. Int. Ed.* **61**, e202212680 (2022).
34. R. Xu, J. Lu, K. Amine, Progress in mechanistic understanding and characterization techniques of Li-S batteries. *Adv. Energy Mater.* **5**, 1500408 (2015).
35. E. Zhao, K. Nie, X. Yu, Y.-S. Hu, F. Wang, J. Xiao, H. Li, X. Huang, Advanced characterization techniques in promoting mechanism understanding for lithium–sulfur batteries. *Adv. Funct. Mater.* **28**, 1707543 (2018).
36. H. L. Wu, L. A. Huff, A. A. Gewirth, In situ raman spectroscopy of sulfur speciation in lithium-sulfur batteries. *ACS Appl. Mater. Interfaces* **7**, 1709–1719 (2015).
37. S. Lang, S.-H. Yu, X. Feng, M. R. Krumov, H. D. Abruña, Understanding the lithium–sulfur battery redox reactions via operando confocal Raman microscopy. *Nat. Commun.* **13**, 4811 (2022).
38. M. Cuisinier, P.-E. Cabelguen, S. Evers, G. He, M. Kolbeck, A. Garsuch, T. Bolin, M. Balasubramanian, L. F. Nazar, Sulfur speciation in Li-S batteries determined by operando X-ray absorption spectroscopy. *J. Phys. Chem. Lett.* **4**, 3227–3232 (2013).
39. M. A. Lowe, J. Gao, H. D. Abruña, Mechanistic insights into operational lithium–sulfur batteries by in situ X-ray diffraction and absorption spectroscopy. *RSC Adv.* **4**, 18347–18353 (2014).
40. Y. Gorlin, M. U. M. Patel, A. Freiberg, Q. He, M. Piana, M. Tromp, H. A. Gasteiger, Understanding the charging mechanism of lithium-sulfur batteries using spatially resolved *operando* X-ray absorption spectroscopy. *J. Electrochem. Soc.* **163**, A930–A939 (2016).
41. X. Li, M. Banis, A. Lushington, X. Yang, Q. Sun, Y. Zhao, C. Liu, Q. Li, B. Wang, W. Xiao, C. Wang, M. Li, J. Liang, R. Li, Y. Hu, L. Goncharova, H. Zhang, T. K. Sham, X. Sun, A high-energy sulfur cathode in carbonate electrolyte by eliminating polysulfides via solid-phase lithium-sulfur transformation. *Nat. Commun.* **9**, 4509 (2018).
42. J. Conder, R. Bouchet, S. Trabesinger, C. Marino, L. Gubler, C. Villevieille, Direct observation of lithium polysulfides in lithium-sulfur batteries using *operando* X-ray diffraction. *Nat. Energy* **2**, 17069 (2017).
43. C. Barchasz, F. Molton, C. Duboc, J. C. Leprêtre, S. Patoux, F. Alloin, Lithium/sulfur cell discharge mechanism: An original approach for intermediate species identification. *Anal. Chem.* **84**, 3973–3980 (2012).
44. S.-H. Yu, X. Huang, K. Schwarz, R. Huang, T. A. Arias, J. D. Brock, H. D. Abruña, Direct visualization of sulfur cathodes: New insights into Li–S batteries *via operando* X-ray based methods. *Energy Environ. Sci.* **11**, 202–210 (2018).
45. X. Yu, H. Pan, Y. Zhou, P. Northrup, J. Xiao, S. Bak, M. Liu, K. W. Nam, D. Qu, J. Liu, T. Wu, X. Q. Yang, Direct observation of the redistribution of sulfur and polysufides in Li–S batteries during the first cycle by in situ X-ray fluorescence microscopy. *Adv. Energy Mater.* **5**, 1500072 (2015).
46. S.-Y. Lang, Y. Shi, Y.-G. Guo, R. Wen, L.-J. Wan, High-temperature formation of a functional film at the cathode/electrolyte interface in lithium–sulfur batteries: An in situ AFM study. *Angew. Chem. Int. Ed.* **56**, 14433–14437 (2017).
47. S.-Y. Lang, Y. Shi, Y.-G. Guo, D. Wang, R. Wen, L.-J. Wan, Insight into the interfacial process and mechanism in lithium–sulfur batteries: An in situ AFM study. *Angew. Chem. Int. Ed.* **55**, 15835–15839 (2016).
48. A. B. Gunnarsdóttir, C. v. Amanchukwu, S. Menkin, C. P. Grey, Noninvasive in situ NMR study of "dead lithium" formation and lithium corrosion in full-cell lithium metal batteries. *J. Am. Chem. Soc.* **142**, 20814–20827 (2020).
49. K. A. See, M. Leskes, J. M. Griffin, S. Britto, P. D. Matthews, A. Emly, A. van der Ven, D. S. Wright, A. J. Morris, C. P. Grey, R. Seshadri, Ab initio structure search and in situ ^{7}Li NMR studies of discharge products in the Li-S battery system. *J. Am. Chem. Soc.* **136**, 16368–16377 (2014).
50. W. Zhou, C. Wang, Q. Zhang, H. D. Abruña, Y. He, J. Wang, S. X. Mao, X. Xiao, Tailoring pore size of nitrogen-doped hollow carbon nanospheres for confining sulfur in lithium-sulfur batteries. *Adv. Energy Mater.* **5**, 1401752 (2015).
51. R. Xu, I. Belharouak, X. Zhang, R. Chamoun, C. Yu, Y. Ren, A. Nie, R. Shahbazian-Yassar, J. Lu, J. C. M. Li, K. Amine, Insight into sulfur reactions in Li-S batteries. *ACS Appl. Mater. Interfaces* **6**, 21938–21945 (2014).
52. M. U. M. Patel, R. Dominko, Application of in *operando* UV/Vis spectroscopy in lithium-sulfur batteries. *ChemSusChem* **7**, 2167–2175 (2014).
53. Q. Zou, Y. C. Lu, Solvent-dictated lithium sulfur redox reactions: An *operando* UV-vis spectroscopic study. *J. Phys. Chem. Lett.* **7**, 1518–1525 (2016).
54. R. Fang, S. Zhao, Z. Sun, D.-W. Wang, H.-M. Cheng, F. Li, More reliable lithium-sulfur batteries: Status, solutions and prospects. *Adv. Mater.* **29**, 1606832 (2017).
55. W. Zhu, A. Paolella, C. S. Kim, D. Liu, Z. Feng, C. Gagnon, J. Trottier, A. Vijh, A. Guerfi, A. Mauger, C. M. Julien, M. Armand, K. Zaghib, Investigation of the reaction mechanism of lithium sulfur batteries in different electrolyte systems by: In situ Raman spectroscopy and in situ X-ray diffraction. *Sustain. Energy Fuels* **1**, 737–747 (2017).
56. J.-T. Yeon, J.-Y. Jang, J.-G. Han, J. Cho, K. T. Lee, N.-S. Choi, Raman spectroscopic and X-ray diffraction studies of sulfur composite electrodes during discharge and charge. *J. Electrochem. Soc.* **159**, A1308–A1314 (2012).
57. M. Hagen, P. Schiffels, M. Hammer, S. Dörfler, J. Tübke, M. J. Hoffmann, H. Althues, S. Kaskel, In-situ raman investigation of polysulfide formation in Li-S cells. *J. Electrochem. Soc.* **160**, A1205–A1214 (2013).
58. T. W. Welch, S. A. Ciftan, P. S. White, H. H. Thorp, Electron-rich oxoruthenium(IV) cleavage agents: A zero-order rate law for DNA catalysis. *Inorg. Chem.* **36**, 4812–4821 (1997).
59. A. W. Jones, A. Eklund, R. Kronstrand, Concentration-time profiles of gamma-hydroxybutyrate in blood after recreational doses are best described by zero-order rather than first-order kinetics. *J. Anal. Toxicol.* **33**, 332–335 (2009).
60. X. Zhou, R. Meng, N. Zhong, S. Yin, G. Ma, X. Liang, Size-dependent cobalt catalyst for lithium sulfur batteries: From single atoms to nanoclusters and nanoparticles. *Small Methods* **5**, 2100571 (2021).
61. J. D. McBrayer, T. E. Beechem, B. R. Perdue, C. A. Apblett, F. H. Garzon, Polysulfide speciation in the bulk electrolyte of a lithium sulfur battery. *J. Electrochem. Soc.* **165**, A876–A881 (2018).
62. X. Gao, X. Zheng, Y. Tsao, P. Zhang, X. Xiao, Y. Ye, J. Li, Y. Yang, R. Xu, Z. Bao, Y. Cui, All-solid-state lithium-sulfur batteries enhanced by redox mediators. *J. Am. Chem. Soc.* **143**, 18188–18195 (2021).
63. Y. Gorlin, A. Siebel, M. Piana, T. Huthwelker, H. Jha, G. Monsch, F. Kraus, H. A. Gasteiger, M. Tromp, *Operando* characterization of intermediates produced in a lithium-sulfur battery. *J. Electrochem. Soc.* **162**, A1146–A1155 (2015).
64. D. R. Wang, D. B. Shah, J. A. Maslyn, W. S. Loo, K. H. Wujcik, E. J. Nelson, M. J. Latimer, J. Feng, D. Prendergast, T. A. Pascal, N. P. Balsara, Rate constants of electrochemical reactions in a lithium-sulfur cell determined by *operando* X-ray absorption spectroscopy. *J. Electrochem. Soc.* **165**, A3487–A3495 (2018).
65. T. A. Pascal, K. H. Wujcik, J. Velasco-Velez, C. Wu, A. A. Teran, M. Kapilashrami, J. Cabana, J. Guo, M. Salmeron, N. Balsara, D. Prendergast, X-ray absorption spectra of dissolved polysulfides in lithium-sulfur batteries from first-principles. *J. Phys. Chem. Lett.* **5**, 1547–1551 (2014).
66. K. H. Wujcik, D. R. Wang, T. A. Pascal, D. Prendergast, N. P. Balsara, In situ X-ray absorption spectroscopy studies of discharge reactions in a thick cathode of a lithium sulfur battery. *J. Electrochem. Soc.* **164**, A18–A27 (2017).
67. P. Wang, Y. Ren, R. Wang, P. Zhang, M. Ding, C. Li, D. Zhao, Z. Qian, Z. Zhang, L. Zhang, L. Yin, Atomically dispersed cobalt catalyst anchored on nitrogen-doped carbon nanosheets for lithium-oxygen batteries. *Nat. Commun.* **11**, 1576 (2020).
68. X. Meng, X. Liu, X. Fan, X. Chen, S. Chen, Y. Meng, M. Wang, J. Zhou, S. Hong, L. Zheng, G. Shi, C. W. Bielawski, J. Geng, Single-atom catalyst aggregates: Size-matching is critical to electrocatalytic performance in sulfur cathodes. *Adv. Sci. (Weinh)* **9**, e2103773 (2022).
69. H. T. Lien, S. T. Chang, P. T. Chen, D. P. Wong, Y. C. Chang, Y. R. Lu, C. L. Dong, C. H. Wang, K. H. Chen, L. C. Chen, Probing the active site in single-atom oxygen reduction catalysts via operando X-ray and electrochemical spectroscopy. *Nat. Commun.* **11**, 4233 (2020).
70. B. Ravel, M. Newville, ATHENA, ARTEMIS, HEPHAESTUS: Data analysis for X-ray absorption spectroscopy using IFEFFIT. *J. Synchrotron Radiat.* **12**, 537–541 (2005).
71. F. Neese, The ORCA program system. *Wiley Interdiscip. Rev. Comput. Mol. Sci.* **2**, 73–78 (2012).
72. M. D. Hanwell, D. E. Curtis, D. C. Lonie, T. Vandermeerschd, E. Zurek, G. R. Hutchison, Avogadro: An advanced semantic chemical editor, visualization, and analysis platform. *J. Cheminform.* **4**, 1–17 (2012).
73. L. Martinez, R. Andrade, E. G. Birgin, J. M. Martínez, PACKMOL: A package for building initial configurations for molecular dynamics simulations. *J. Comput. Chem.* **30**, 2157–2164 (2009).
74. W. Humphrey, A. Dalke, K. Schulten, VMD: Visual molecular dynamics. *J. Mol. Graph.* **14**, 33–38 (1996).
75. S. Gu, S. Xu, X. Song, H. Li, Y. Wang, G. Zhou, N. Wang, H. Chang, Electrostatic potential-induced Co–N_4 active centers in a 2D conductive metal-organic framework for high-performance lithium-sulfur batteries. *ACS Appl. Mater. Interfaces* **14**, 50815–50826 (2022).

Acknowledgments

Funding: This work was supported by the Cornell Energy System Institute (CESI), Daimler/Mercedes-Benz. This work made use of TEM and Raman facilities at the Cornell Center for Materials Research (CCMR), which are supported through the National Science Foundation Materials Research Science and Engineering Center (NSF MRSEC) program (DMR-1719875). This research used 8-BM of the National Synchrotron Light Source II, a U.S. Department of Energy (DOE) Office of Science User Facility operated for the DOE Office of Science by Brookhaven National Laboratory under contract no. DE-SC0012704. S.-M.B. acknowledge support (in part) from the New Faculty Research Seed Funding Grant of Yonsei University. This work is based on research conducted at the Center for High-Energy X-ray Sciences (CHEXS), which is supported

by the National Science Foundation (BIO, ENG, and MPS Directorates) under award DMR-1829070. **Author contributions:** W.X., S.L., and H.D.A. conceived and designed the project. W.X. performed sample preparation, structural characterization, and electrochemical measurements. R.Z. helped with STEM and XPS. W.X. and S.L. conducted operando confocal Raman and XAS experiments with the help of H.L. and M.R.K. W.X. and S.L. performed XAS data analysis with the help of X.F., S.-M.B., C.J.P., and Y.D. K.W. and J.Y. conducted the theoretical calculations. W.X., S.L., and H.D.A. wrote the manuscript. All of the authors discussed the results and commented on the manuscript. **Competing interests:** The authors declare that they have no competing interests. **Data and materials availability:** All data needed to evaluate the conclusions in the paper are present in the paper and/or the Supplementary Materials.

Submitted 1 May 2023
Accepted 14 July 2023
Published 16 August 2023
10.1126/sciadv.adi5108